Photonics-Based Superresolution Radar Imaging With Space-Time-Frequency Coincidence Processing

Xiaoyue Yu, Qing Xiong, Fangzheng Zhang, *Senior Member, IEEE*, Xin Yan, Yansen He, *Student Member, IEEE*, Gong Zhang, *Senior Member, IEEE*, Xiangchuan Wang, Zhenyu Xu, Biao Xu, and Shilong Pan, *Fellow, IEEE*

***Abstract*—A photonics-based, superresolution radar imaging system using space-time-frequency coincidence processing is proposed and experimentally demonstrated. In the transmitter, a broadband, frequency-hopping (FH) signal is generated by an optically injected semiconductor laser based on the P1 oscillation dynamics. The generated signal is switched and transmitted through a uniform linear antenna array (ULA) by means of time division multiplexing (TDM). Therein, a space-time-frequency, 3-D stochastic radiation field is constructed, which is manifested as wavefront modulation. In the receiver, the radar echoes are received and frequency downconverted to baseband through IQ mixing. Thanks to the broadband operation capability of the microwave photonic system, high range resolution can be easily achieved. To overcome the azimuth resolution limitation determined by the array aperture size, a kernel function-based sparse reconstruction algorithm is proposed, which enables superresolution coincidence imaging in the azimuth direction. In the experiments, a photonics-based 4 $\times$ 1 multiple-input single-output (MISO) radar with a bandwidth of 8 GHz (10–18 GHz) is established, in which the transmitted signal is a 32-level FH signal. Combined with the proposed coincidence imaging algorithm, superresolution radar imaging is realized with the range-azimuth imaging resolution reaching 2.3 $\times$ 0.8 cm, which surpasses that of the traditional MISO radar by 20 times in azimuth resolution. In addition, the imaging experiments of complex targets with N, V, and A shapes and an aircraft model with a continuous structure are demonstrated to imitate real scenes, which verify the feasibility of the proposed photonics-based radar system in high-resolution forward-looking imaging.**

***Index Terms*—Coincidence imaging, microwave photonics, optical injection, radar, semiconductor laser.**

Received 8 January 2026; revised 9 April 2026; accepted 1 June 2026. Date of publication 3 June 2026; date of current version 11 June 2026. This work was supported in part by the National Natural Science Foundation of China under Grant 62371224, Grant 62271255, and Grant 62501504; in part by Shanghai Aerospace Science and Technology Innovation Fund under Grant SAST2024-023; in part by Shenzhen Science and Technology Program under Grant JCYJ20210324134807019; in part by the Postgraduate Research and Practice Innovation Program of Jiangsu Province under Grant KYCX24_0580; in part by the Postgraduate Research and Practice Innovation Program of Jiangsu Province under Grant KYCX25_0591; in part by the Foundation for Cultivated Young Talents of Fujian Province under Grant 2025350068; and in part by the Fundamental Research Funds for the Central Universities under Grant 2072025016. *(Xiaoyue Yu and Qing Xiong contributed equally to this article.) (Corresponding authors: Fangzheng Zhang; Gong Zhang.)*

Xiaoyue Yu, Qing Xiong, Fangzheng Zhang, Xin Yan, Yansen He, Gong Zhang, Xiangchuan Wang, and Shilong Pan are with the National Key Laboratory of Microwave Photonics, Nanjing University of Aeronautics and Astronautics, Nanjing 210016, China (e-mail: zhangfangzheng@nuaa.edu.cn; gzhang@nuaa.edu.cn).

Zhenyu Xu is with Shanghai Institute of Satellite Engineering, Shanghai 200240, China.

Biao Xu is with the Key Laboratory of Underwater Acoustic Communication and Marine Information Technology, Ministry of Education, Xiamen University, Xiamen 361005, China.

Digital Object Identifier 10.1109/TRS.2026.3699825

I. Introduction

RADAR is a popular method for all-time and all-weather target detection that has attracted tremendous attention in the fields of air traffic control, remote sensing, disaster relief, combat surveillance, and so on [1]. With the increasing complexity of the detection environment, high-resolution radar imaging in both the range and azimuth dimensions is in higher demand. The range resolution and azimuth resolution are mainly determined by the operating bandwidth and aperture size of the radar, respectively. However, traditional real aperture radar based on an electrical signal generator (ESG) usually suffers from a limited bandwidth. In addition, azimuth resolution typically comes at the price of a large array aperture size. To achieve high-resolution radar imaging, microwave array radars have been developed to expand the equivalent aperture size, including multiple-input single-output (MISO) radars, multiple-input multiple-output (MIMO) radars [2], [3], and phased array radars, etc. While the azimuth resolution is constrained by the Rayleigh limitation determined by the aperture size. A good solution to cope with this problem is coincidence imaging [4], [5], [6], [7], [8], [9], which has superresolution imaging capability by transmitting a temporal–spatial stochastic radiation field and reconstructing the image by coincidence processing. However, limited by the bandwidth of ESGs, the reconstructed azimuth superresolution is still limited, making it challenging to precisely identify small targets. To further enhance the detection capability of the radar system, in recent years, microwave photonic techniques have been introduced to radar systems leveraging the inherent advantages of photonics, such as fast signal processing, ultrawide bandwidth, a flat spectral response, and electromagnetic interference immunity [10], [11], [12], [13], [14], [15]. Compared with traditional electronic radars, microwave photonic radars significantly enhance the signal processing bandwidth and provide more possibilities by performing multiplexing in time [16], [17], [18], [19], wavelength [20], [21], [22], and polarization [23], [24] domains. Thus, the stochastic radiation field in coincidence imaging could be

2832-7357 © 2026 IEEE. All rights reserved, including rights for text and data mining, and training of artificial intelligence and similar technologies. Personal use is permitted, but republication/redistribution requires IEEE permission. See https://www.ieee.org/publications/rights/index.html for more information.

Authorized licensed use limited to: NANJING UNIVERSITY OF AERONAUTICS AND ASTRONAUTICS. Downloaded on July 20,2026 at 09:35:34 UTC from IEEE Xplore. Restrictions apply.

TABLE I
COMPARISON OF THE STATE-OF-THE-ART ARRAY RADAR IMAGING SYSTEMS

Reference	Signal generation method	System structure	Bandwidth	Imaging method	Imaging resolution	Super-resolution capability
[8]	Vector network analyzer	11×11 MIMO	2 GHz (33-35 GHz)	Coincidence imaging	10 cm×30 cm	Super-resolution factor: 1.7
[9]	Direct digital synthesizers	10×1 MISO	0.25 GHz (9.175-9.425 GHz)	Coincidence Imaging	40 cm×0.0058 rad	Super-resolution factor: 4.39
[16]	Photonics frequency quadrupling	4×1 MISO	4 GHz (22-26 GHz)	Digital beamforming	3.85 cm×2.68°	No super-resolution capability
[18]	Photonics frequency quadrupling	8×8 MIMO	8 GHz (18-26 GHz)	Digital beamforming	2 cm×2°	No super-resolution capability
[20]	Optical heterodyning	4×8 MIMO	8 GHz (18-26 GHz)	Back-projection algorithm	7.5cm×1.85°	No super-resolution capability
[25]	Optical injection semiconductor laser	8×8 MIMO	8 GHz (18-26 GHz)	Coincidence Imaging (Wave-post modulation)	2 cm×0.3°	Super-resolution factor: 6
This work	Optical injection semiconductor laser	4×1 MISO	8 GHz (10-18 GHz)	KFSR algorithm	2.3 cm × 0.8 cm	Super-resolution factor: 20

extended from space-time dimensions to space-time-frequency dimensions based on microwave photonics. Considering that the superresolution factor is proportional to the randomness of the stochastic radiation field, it is a good way to improve the radar detection capability by combining the large bandwidth and multidimensional multiplexing of microwave photonics with the superresolution capability of coincidence imaging processing.

Previously, a photonics-based MIMO radar incorporating a digital coincidence imaging method was proposed to implement superresolution radar imaging [25]. However, the transmitted signals are the same in different transmitting channels, resulting in weak diversity in the stochastic radiation field. To achieve coincidence imaging, random phase modulation processing is applied to the received echoes, which is manifested as wave-post modulation and does not fully exploit the advantages of microwave photonics.

In this article, we propose a photonics-based superresolution radar imaging system based on a space-time-frequency stochastic radiation field. In the transmitter, broadband frequency-hopping (FH) signals are generated by an optically injected semiconductor laser based on the P1 oscillation dynamics. The frequency of the generated microwave signal can be continuously tuned from several gigahertz to tens of gigahertz, which provides broadband microwave sources to fulfill the high-resolution radar demand [26], [27], [28], [29], [30], [31], [32]. In addition, the frequency switching time in an optically injected semiconductor laser is on the ns-level, and the P1 oscillation frequency is approximately linear with the injection strength. Thus, by adjusting the injection parameters, the generated FH signals can have both high frequency accuracy and excellent reconfigurability. The generated signal is switched and transmitted through a uniform linear antenna array (ULA) by time-division multiplexing (TDM). Therein, frequency coding of each subpulse is specially designed, which ensures the otherness and orthogonality of transmitting signals between multichannels. Based on this, a space-time-frequency 3-D stochastic radiation field is constructed, which is manifested as wavefront modulation. In the receiver, the radar echoes are received by a single antenna and frequency downconverted to baseband through electrical IQ mixing. Furthermore, to achieve superresolution radar imaging, a kernel function-based sparse reconstruction (KFSR) algorithm is proposed to effectively overcome the azimuth resolution limitation of the array aperture. In the experiments, a photonics-based 4×1 MISO radar system is conducted. The signal of each transmitting channel is a 32-level random FH signal with an instantaneous bandwidth covering 10–18 GHz, of which the range resolution reaches 2.13 cm. Combined with the proposed KFSR algorithm, superresolution radar imaging is realized. The azimuth superresolution reaches 0.8 cm, which surpasses the traditional MISO radar by 20 times in azimuth resolution. Furthermore, the imaging experiments on complex targets with N, V, and A shapes and an aircraft model with a continuous structure are demonstrated to imitate real scenes. In addition, to clearly compare the effectiveness of the proposed scheme, Table I summarizes the performance of the state-of-the-art array radar imaging systems. Compared with the microwave coincidence processing radar reported in [8] and [9], the introduction of microwave photonics significantly increases the bandwidth of the transmitted signal, thus enabling better range resolution. In addition, benefiting from the superresolution imaging capability of the proposed KFSR algorithm, the photonics-based radar in this work achieves a higher superresolution factor. Consequently, the proposed space-time-frequency imaging radar offers a promising solution to overcome the Rayleigh limitation determined by the aperture size, making it well-suited for high-resolution forward-looking imaging applications.

The subsequent sections of this article are structured as follows. Section II introduces the principles of the proposed photonics-based MISO radar and algorithm. In Section III, the experimental setup of the photonics-based broadband 4×1

Authorized licensed use limited to: NANJING UNIVERSITY OF AERONAUTICS AND ASTRONAUTICS. Downloaded on July 20,2026 at 09:35:34 UTC from IEEE Xplore. Restrictions apply.

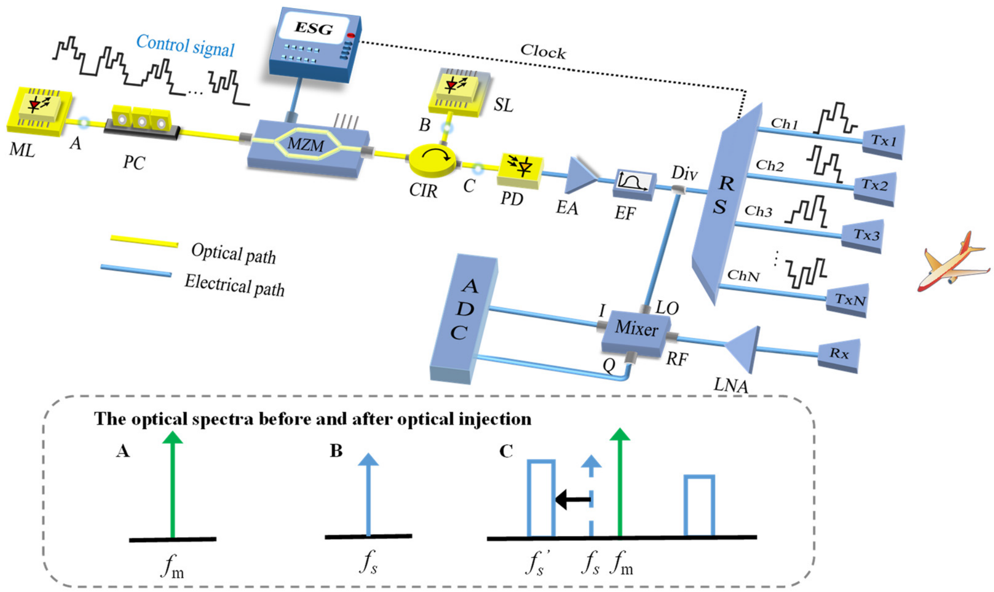

Fig. 1. Scheme of the proposed photonics-based MISO radar system. ML: master laser, PC: polarization controller, MZM: Mach–Zehnder modulator, ESG: electrical signal generator, CIR: optical circulator, SL: slave laser, PD: photodetector, EA: electrical amplifier, EF: electrical filter, Div: divider, RS: RF switch, Tx: transmitting antenna, Rx: receiving antenna, LNA: low noise amplifier, Mixer: electrical IQ mixer, and ADC: analog digital converter.

MISO radar system is discussed, and superresolution radar imaging is verified. Finally, Section IV concludes.

II. Principle

A. System Configuration

Fig. 1 shows the structure of the photonics-based MISO radar system. The frequency-hopping signals are generated through an optically injected semiconductor laser based on the P1 oscillation dynamics. The continuous light emitted by the master laser (ML) with a wavelength of f_{m} is injected into a slave laser (SL) after passing through a polarization controller (PC) and an optical circulator (CIR). The free-running wavelength of the SL is f_{s}. The optical spectra of the ML and free-running SL before optical injection are shown at points a and b in Fig. 1. Under proper injection parameters, the P1 oscillation is invoked in the cavity of the SL. The P1 oscillation frequency can be broadly tuned from several gigahertz to tens of gigahertz and exhibits quasi-linearly with the power of externally injected light, which sets the scene for generating broadband frequency-modulated signals by adjusting the injection power [33]. Thus, a Mach–Zehnder modulator (MZM) is inserted into the system to vary the optical injection strength through optical intensity modulation according to a specially designed control signal generated by a low-speed ESG. After optical injection, the output signal from the SL consists of a regenerated optical carrier and red-shifted optical sidebands, as indicated by the optical spectra at point c in Fig. 1. The wavelength of the SL is broadened and red shifted from f_{s} to f_{s}’. When the control signal loaded on the MZM is programmed to have a multilevel profile, a broadband FH signal is generated after optical-to-electrical conversion by a photodetector (PD). The generated FH signal is amplified by an electrical amplifier (EA) and filtered by an electrical bandpass filter (EF). Subsequently, the FH signal is partitioned into two branches by an electrical divider (Div). In one branch, the signal is sent to the LO port of an electrical mixer, serving as the reference signal for the radar receiver. The FH signal in the other branch is input into a $1 \times N$ RF switch (RS), through which it is switched into N channels in a TDM manner. The radar pulses after the RS are transmitted by a ULA composed of N antennas (Tx). Another antenna (Rx) is used to collect the radar echoes. Therein, to ensure the orthogonality of the transmitted signals in different channels, the loaded control signal is specially designed so that the frequency coding of the radar pulse in each channel is different. So far, a photonics-based, space-time-frequency, 3-D stochastic radiation field is constructed.

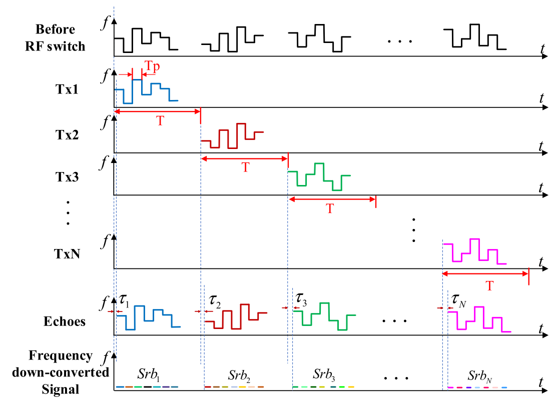

Fig. 2. Transmitting and receiving temporal sequence diagrams of the proposed MISO radar.

The detailed temporal sequence diagram based on the proposed MISO radar is illustrated in Fig. 2. The switching time between adjacent channels equals the temporal period T of the transmitted radar pulse. The transmitted signal St_n in the nth channel is expressed as follows:

$$S\,t_n\,(t) = \sum_{k=0}^{K-1} rect\left(\frac{t - kT_p}{T_p}\right) \exp\left[j2\pi\left(f_c + f_{n,k}\right)t\right] \qquad (1)$$

Authorized licensed use limited to: NANJING UNIVERSITY OF AERONAUTICS AND ASTRONAUTICS. Downloaded on July 20,2026 at 09:35:34 UTC from IEEE Xplore. Restrictions apply.

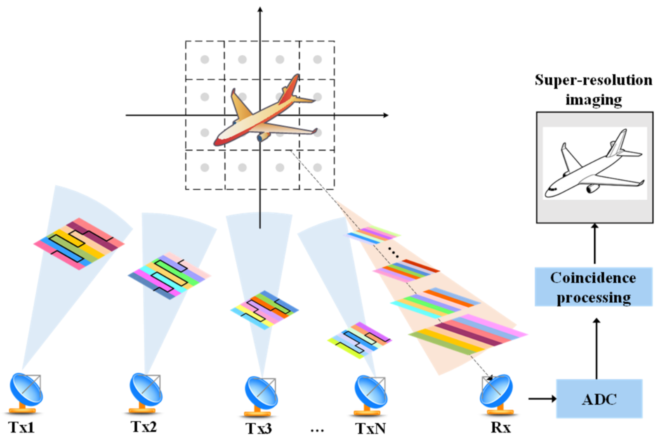

Fig. 3. Principle of the proposed photonics-based coincidence imaging radar.

where n $(n = 1, 2, \ldots, N)$ is the transmitting channel index, k $(k = 0, 2, \ldots, K-1)$ is the subpulse index, and K is the total number of FH points. $T_p = T * \eta/K$ is the subpulse duration, and η is the duty cycle of the transmitting signal, which is consistent for each transmitting channel. f_{c} is the carrier frequency, and $f_{\mathrm{n,k}}$ is the frequency-hopping range of the kth subpulse in the nth transmitting channel corresponding to the carrier frequency.

To ensure the orthogonality of the transmitted signal in different channels, the frequency $f_{\mathrm{n,k}}$ should be constrained to satisfy [34]

$$f_{n,k} \neq f_{n',k}, \quad \text{for } n \neq n' \quad \forall k. \tag{2}$$

In the receiver, the radar echoes collected by a single antenna are amplified by a low-noise amplifier (LNA) before being launched to the RF port of the electrical IQ mixer for frequency downconversion. This processing is also illustrated in Fig. 2. Benefiting from the large bandwidth of photonics, the uncorrelation of the radiation field at any two target positions is extremely enhanced in the frequency domain. By adjusting the amplitude of the electrical control signal, condition (2) is easily satisfied, thereby improving the fluctuating characteristics of the wavefront. Thus, the targets irradiated by the stochastic radiation field reflect spatial–temporal-spectral diversity echoes associated with their respective positions. When the echoes are frequency downconverted to baseband, the target information is contained in the phase domain, which leads to a significant reduction of the required sampling rate. The I channel and Q channel signals from the electric mixer are recorded by a real-time oscilloscope (OSC) as an analog-to-digital converter (ADC). Subsequently, digital signal processing is performed to get the target information.

B. KFSR Algorithm

To realize superresolution radar imaging, a coincidence imaging method for a space-time-frequency stochastic radiation field is proposed, of which the principle is shown in Fig. 3. The imaging area is a 2-D plane located in the line-of-sight direction of the radar, which is uniformly divided into L imaging grids. Assuming all scattering points of the targets are located at the center of the imaging grid units, the scattering coefficient vector $\boldsymbol{\sigma}$ in the imaging grids is expressed as follows:

$$\boldsymbol{\sigma} = [\boldsymbol{\sigma}_1, \boldsymbol{\sigma}_2, \ldots, \boldsymbol{\sigma}_L]^T \tag{3}$$

when there is no scatterer in the lth imaging grid, $\sigma_l = 0$.

Based on the proposed MISO radar system, the received echo signal for the nth transmitting antenna can be written as follows:

$$\begin{aligned} Sr_n^l(t) &= \sum_{l=1}^{L} \sigma_l \sum_{k=0}^{K-1} rect\left(\frac{t - kT_p - \frac{R_{ntr}(l)}{c}}{T_p}\right) \exp\left[j2\pi\left(f_c + f_{n,k}\right)t\right] \\ &\quad \cdot \exp\left[-j2\pi\left(f_c + f_{n,k}\right)\frac{R_{ntr}(l)}{c}\right] \end{aligned} \tag{4}$$

where c is the speed of light, $R_{ntr}(l)$ is the two-way propagation distance of the nth transmitting channel reaching the lth imaging grid and received by the receiving antenna. Benefiting from the wavefront modulation of the transmitted signal, the detection signal in different imaging grids has space-time-frequency diversity, thereby providing the possibility of superresolution imaging.

After IQ mixing, the received echo signals are frequency downconverted to baseband, which is expressed as follows:

$$\begin{aligned} Srb_n^l(t) = \sum_{l=1}^{L} \sigma_l \sum_{k=0}^{K-1} rect\left(\frac{t - kT_p - \frac{R_{ntr}(l)}{c}}{T_p}\right) \\ \cdot \exp\left[-j2\pi\left(f_c + f_{n,k}\right)\frac{R_{ntr}(l)}{c}\right]. \end{aligned} \tag{5}$$

Then, the baseband echo signal in (5) is discretized, which is expressed as follows:

$$Srb_n^l(m) = \sum_{l=1}^{L} \widetilde{\sigma}_l \sum_{k=0}^{K-1} u\left(m - kf_sT_p\right) \exp\left[-j2\pi f_{n,k}\frac{R_{ntr}(l)}{c}\right] \tag{6}$$

where m is the sampling point of the frequency downconverted echo signal $(m = 1, 2, \ldots, M,\ M = Kf_sT_p)$. f_s is the sampling rate of the baseband echo signal. $u(\mathrm{x}) = 1$ for $0 \leq x \leq f_sT_p$. $\tilde{\sigma}_l$ is the complex scattering coefficient, which is expressed as follows:

$$\tilde{\sigma}_l = \sigma_l \exp\left[-j2\pi f_c \frac{R_{ntr}(l)}{c}\right]. \tag{7}$$

Without loss of generality, the targets can be regarded as several ideal point scattering centers, which are much less than the number of imaging grids and shows the a priori spatial–temporal-spectral sparsity [6], [35]. Thus, to achieve azimuth superresolution, a coincidence imaging algorithm is introduced. However, the propagation delay of the scatterer in each imaging grid is reflected in the phase of the baseband receiving signal. For the proposed radar, the obtained baseband signal is related to the frequency coding of the transmitted signal. The traditional imaging method based on the Fourier transformation (FFT) cannot be applied. To address this problem, the KFSR algorithm is applied to further improve the radar imaging performance in the azimuth dimension, which is

Authorized licensed use limited to: NANJING UNIVERSITY OF AERONAUTICS AND ASTRONAUTICS. Downloaded on July 20,2026 at 09:35:34 UTC from IEEE Xplore. Restrictions apply.

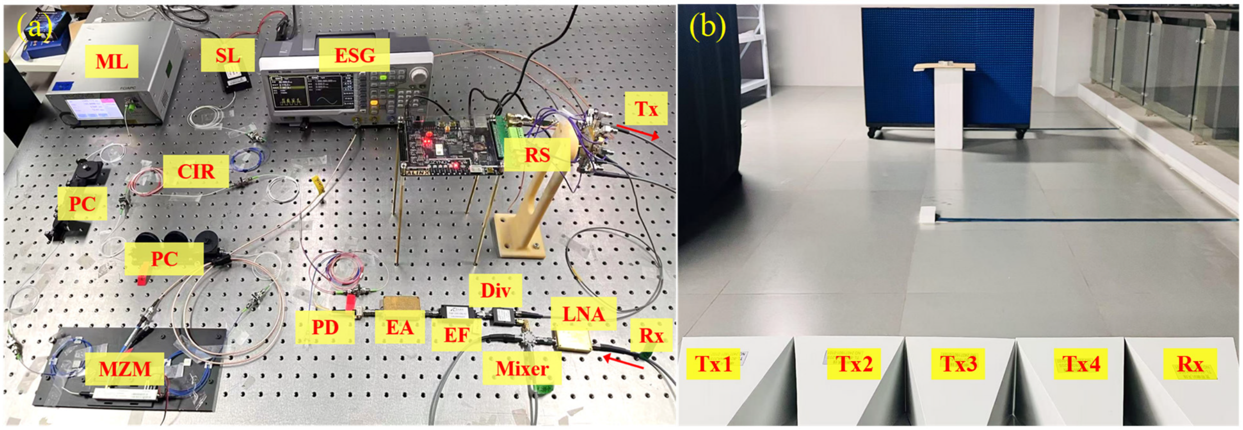

Fig. 4. Photographs of (a) established photonics-based MISO radar and (b) detection scenario.

composed of a series of reference signals with variable phases determined by the spatial positions of imaging grids [29], [36]. Thus, the discretized observing signal in the lth imaging grid with respect to the nth transmitting channel can be constructed based on the KFSR algorithm

$$\kappa_{n,l}(m) = \sum_{k=0}^{K-1} u\left(m - k f_s T_p\right) \exp\left[-j2\pi f_{n,k} \frac{R_{ntr}(l)}{c}\right]. \quad (8)$$

Then, the frequency downconverted echo signal of the nth transmitting channel corresponding to the imaging area can be represented as follows:

$$Srb_{\boldsymbol{n}} = \boldsymbol{\kappa_n} \tilde{\boldsymbol{\sigma}} + \boldsymbol{W_n} \quad (9)$$

where $\boldsymbol{\kappa_n} = [\kappa_{n,1}^{\mathrm{T}}, \kappa_{n,2}^{\mathrm{T}}, \ldots, \kappa_{n,L}^{\mathrm{T}}]$ is the constructed kernel function with respect to the nth transmit channel, and $\boldsymbol{W_n}$ is the Gaussian white noise vector. Compared with the classic coincidence imaging algorithm, the proposed KFSR algorithm replaces the reference matrix constructed from the transmitted signal and avoids the acquisition of broadband signals, leading to a substantial reduction in computational complexity. Thus, (9) can be expanded to be

$$\begin{bmatrix} Srb_n(1) \\ Srb_n(2) \\ \vdots \\ Srb_n(M) \end{bmatrix} = \begin{bmatrix} \kappa_{n,1}(1) & \kappa_{n,2}(1) & \cdots & \kappa_{n,L}(1) \\ \kappa_{n,1}(2) & \kappa_{n,2}(2) & \cdots & \kappa_{n,L}(2) \\ \vdots & \vdots & \ddots & \vdots \\ \kappa_{n,1}(M) & \kappa_{n,2}(M) & \cdots & \kappa_{n,L}(M) \end{bmatrix} \begin{bmatrix} \tilde{\sigma}_1 \\ \tilde{\sigma}_2 \\ \vdots \\ \tilde{\sigma}_L \end{bmatrix} + \boldsymbol{W_n}. \quad (10)$$

Stacking the echo data of the multitransmitting channels, the frequency downconverted echo signal model $\boldsymbol{Srb}$ of N transmitting channels can be expressed as follows:

$$\boldsymbol{Srb} = \boldsymbol{\kappa} \tilde{\boldsymbol{\sigma}} + \boldsymbol{w} \quad (11)$$

where $\boldsymbol{Srb} = [\boldsymbol{Srb}_1^{\mathrm{T}}, \boldsymbol{Srb}_2^{\mathrm{T}} \ldots, \boldsymbol{Srb}_N^{\mathrm{T}}]^{\mathrm{T}}$, $\boldsymbol{\kappa} = [\boldsymbol{\kappa}_1^{\mathrm{T}}, \boldsymbol{\kappa}_2^{\mathrm{T}}, \ldots, \boldsymbol{\kappa}_N^{\mathrm{T}}]^{\mathrm{T}}$ denotes the kernel function of N transmitting channels with respect to the imaging plane. Under the prior condition that the targets are sparse, the wavefront modulation naturally makes the constructed observation matrix satisfy the restricted isometry property (RIP) condition [4]. Then the target imaging can be obtained by the proposed KFSR algorithm

$$\hat{\boldsymbol{\sigma}} = \arg\min \left\{ \|\boldsymbol{Srb} - \boldsymbol{\kappa}\tilde{\boldsymbol{\sigma}}\|_2^2 + \boldsymbol{\lambda}\|\tilde{\boldsymbol{\sigma}}\|_1 \right\} \quad (12)$$

where λ is the regularization parameter, which can balance the reconstruction accuracy and the sparsity of the solution. Thus, by properly adjusting the regularization parameter, the proposed KFSR algorithm can effectively suppress the background noise and retain the real target information. The first term on the right side of the imaging model (12) is a data fidelity term, which incorporates the receiving signal model in (11). The second term contains prior information related to the distribution of scatterers. Thus, the problem in (12) is a basis pursuit denoising problem, which could be solved by convex optimization algorithms [37]. It should be noted that the proposed KFSR ignores the impact of target motion. For a moving target, additional velocity compensation techniques need to be further integrated to enhance its applicability [38].

III. Experiment Results

A photonics-based 4×1 MISO radar experiment is carried out based on the setup in Fig. 1. The detailed experimental system is shown in Fig. 4(a). The corresponding detection scenario is depicted in Fig. 4(b). A tunable laser (ID Photonics, CoBrite) is applied as the ML with a wavelength of 1549.719 nm. Then, the optical signal is input into an MZM (Fujitsu, FTM7937EZ, Bandwidth: 40 GHz) for intensity modulation. The SL is a commercial distributed-feedback semiconductor laser (Wave Optics, DFBM-1550-10-SM-ISN). Its bias current and temperature are set to 21 mA and 27.45 °C, respectively. Therein, a low-speed ESG (RIGOL DG4062, 500 MSa/s) is introduced to produce a control signal in a TDM manner. To construct frequency-domain orthogonal signals, the control signals for different transmitted channels are specially designed to generate 32-level random frequencies with a temporal period of 20 μs, following the orthogonality condition specified in (2). The cross-correlation peak between different pulses remains below 0.1. In the experiment, the corresponding amplitude of the control signal is changed from 1.51 to 2.95 V. In addition, the minimum level of the control signal is set to 1 V to achieve a tunable duty cycle, which is depicted in Fig. 5(a). After optical-to-electrical conversion by a PD (Discovery, DSC40S, 20 GHz), a broadband FH signal is generated and boosted by an EA (TLLA1G18G-50–30). Subsequently, the generated signal is filtered by a bandpass

Authorized licensed use limited to: NANJING UNIVERSITY OF AERONAUTICS AND ASTRONAUTICS. Downloaded on July 20,2026 at 09:35:34 UTC from IEEE Xplore. Restrictions apply.

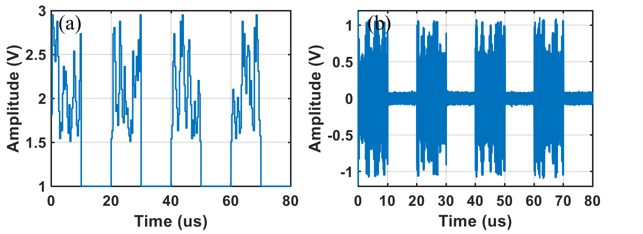

Fig. 5. (a) Control signal and (b) temporal waveform of the generated FH signal.

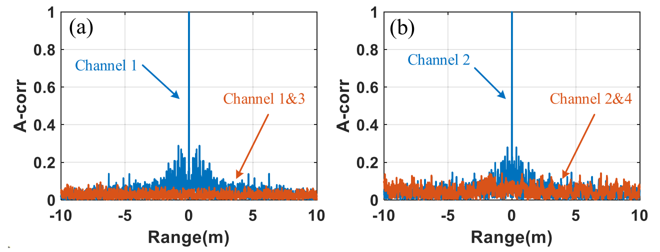

Fig. 7. Autocorrelation and cross-correlation results of temporal waveforms in (a) channel 1 and channel 3 and (b) channel 2 and channel 4.

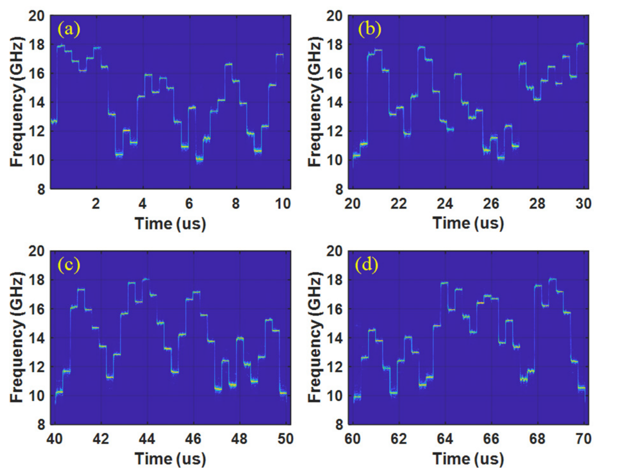

Fig. 6. Detailed time-frequency diagrams of (a) channel 1, (b) channel 2, (c) channel 3, and (d) channel 4.

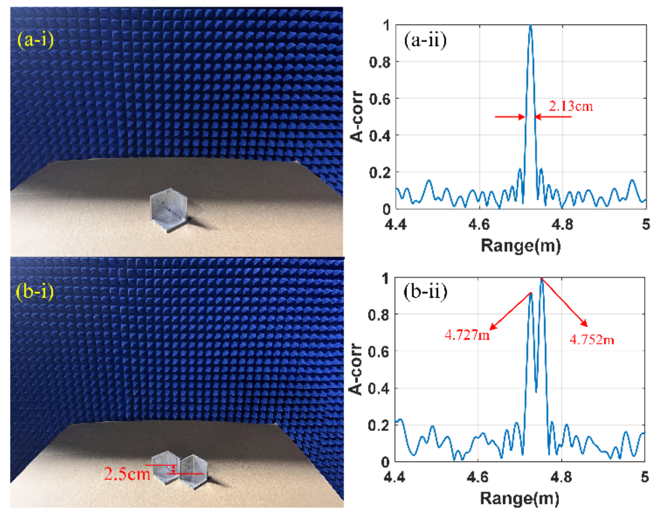

Fig. 8. (i) Photograph of the imaging scenario and (ii) range profile of (a) single target and (b) two targets.

EF (TLBF-10G-18G-x2) and captured by a real-time OSC (Keysight DSO-X, 92504A). The corresponding temporal waveform is depicted in Fig. 5(b), which exhibits a pulsewidth of 80 μs and a duty cycle of 50%.

Then, an RS (Talent Microwave, TLSP8T8G26) is used to split the generated signal into four transmitted channels according to the TDM principle. Here, a 10-MHz crystal oscillator as the clock is utilized to synchronize the control signal and RS. The switching time between adjacent transmitting channels is set to 20 μs, which equals the temporal period of the transmitted pulses. Four horn antennas (6–18 GHz) apart by 12.5 cm in the radar azimuth direction are used to transmit the generated signal to the detection space. Fig. 6(a)–(d) shows the detailed time-frequency diagrams of radar pulses in different transmitting channels obtained by performing a short-time FFT on the sampled temporal waveform. It is observed that the frequency coding in different transmitting channels is different. Each transmitting pulse has 32 random discrete frequencies, covering a bandwidth of 8 GHz (10–18 GHz). To validate the orthogonality among transmitting signals in different channels, the autocorrelation and cross-correlation results between any two transmitting channels are given, as shown in Fig. 7. Fig. 7(a) shows the autocorrelation result (blue lines) of the signal in transmitting channel 1 and the cross-correlation result (orange line) between the signals in transmitting channels 1 and 3. Fig. 7(b) shows the corresponding results between the signals in transmitting channels 2 and 4. It is observed that autocorrelation peaks are significantly higher than cross-correlation peaks, proving the otherness of signals in different transmitted channels.

In the receiver, the echoes are collected by another horn antenna (6–18 GHz) combined with an LNA (AT Microwave, LNA-0242-4004, 2–42 GHz). After frequency mixing in an IQ mixer (Marki MMIQ-0626L, 6–26 GHz), the output I and Q signals are recorded by a multichannel OSC, both with a sampling rate of 500 MSa/s.

First, the range resolution of radar detection based on the proposed system is investigated. A trihedral reflector (edge length: 3 cm) is employed to simulate an ideal point target. When the trihedral reflector is placed forward along the radar line-of-sight direction, its scattering center is located on the virtual vertex formed by three mutually perpendicular reflection surfaces. In the experiment, the target is placed about 4.7 m away from the antenna array. The corresponding detection scenario is depicted in Fig. 8(a-i). Especially, in the experiment, the antenna and the target are placed at the same height; the elevation direction could be regarded as 0°. By performing the kernel function correlation method based on a single-channel signal, the range profile is obtained and depicted in Fig. 8(a-ii). A strong peak centered at 4.722 m appears, which corresponds to the real distance of a single target. The full-width at half-maximum of the peak is measured as 2.13 cm, which is close to the theoretical range resolution.

Authorized licensed use limited to: NANJING UNIVERSITY OF AERONAUTICS AND ASTRONAUTICS. Downloaded on July 20,2026 at 09:35:34 UTC from IEEE Xplore. Restrictions apply.

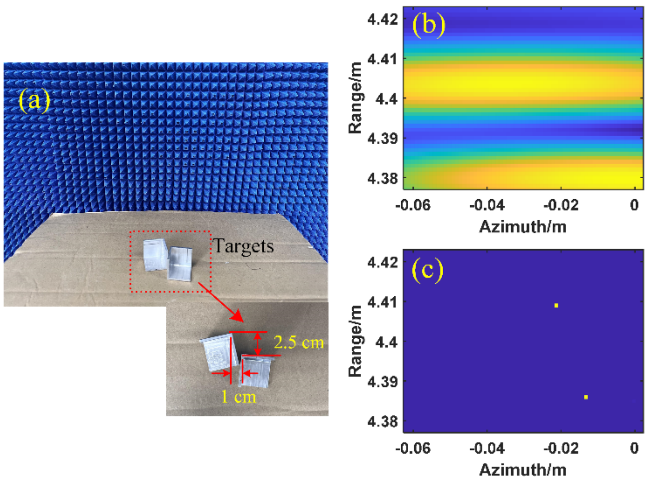

Fig. 9. (a) Photograph of the imaging scenario of two targets, (b) imaging result based on kernel function-based correlation algorithm, and (c) superresolution imaging result based on the proposed KFSR algorithm.

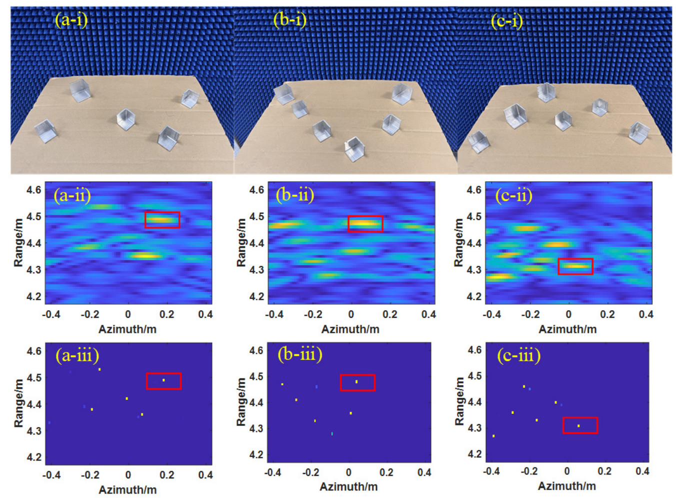

Fig. 10. (i) Photographs of the imaging scenario and the imaging results of (a) N-shaped, (b) V-shaped, and (c) A-shaped complex targets based on (ii) kernel function-based correlation algorithm and (iii) proposed KFSR algorithm.

In addition, the range detection of two targets is carried out, in which two trihedral reflectors are separated by 2.5 cm following the detection path, as illustrated in Fig. 8(b-i). The range profile is depicted in Fig. 8(b-ii). Two distinguishable peaks matching the two targets emerge at 4.727 and 4.752 m, respectively. The distance between the two peaks is measured as 2.5 cm, which is in line with the real values. Again, the results prove the viability of the established FH radar system in high-resolution ranging.

Next, a 2-D imaging experiment based on the proposed system is carried out to validate the feasibility of superresolution imaging. The detection scenario is depicted in Fig. 9(a). To approach the azimuth resolution limitation, two trihedral reflectors (edge length: 3 cm) are placed forward along the detection path. The distances of the two reflectors in the range and azimuth directions are about 2.5 and 1 cm, respectively. It should be noted that the proposed system remains in a stationary position relative to the target during the experiment. For ease of comparison, the target imaging is first constructed by the kernel function-based correlation method. The corresponding imaging result is shown in Fig. 9(b). It is observed that the obtained image has a limited azimuth resolution ρ, which is determined by the array aperture size of the MISO radar. It is calculated by the following equation:

$$\rho \approx 0.886 \frac{cR}{f_c D} \tag{13}$$

where R is the distance from the radar to the target, and D is the array aperture size. In this article, the array aperture of the established MISO radar antennas is 50 cm in the azimuth direction; the corresponding theoretical azimuth resolution ρ is about 16.71 cm, which is much larger than the actual target ranges in the azimuth direction, resulting in the targets in Fig. 9 not being distinguished in the azimuth direction. Furthermore, to break the Rayleigh limit in azimuth resolution, the proposed KFSR algorithm is applied. In the experiment, to achieve optimal performance in terms of target reconstruction fidelity and background suppression, the regularization parameter λ is set to 7. The imaging area is set as a 2-D plane around the targets with a size of 0.047 m (range) $\times$ 0.065 m (azimuth), which is divided into 47 (range) $\times$ 65 (azimuth) units. The corresponding imaging result is shown in Fig. 9(c). Two targets are clearly distinguished in the range and azimuth directions. The measured distances in the range and azimuth directions are 2.3 and 0.8 cm, respectively, which agree well with the real values and prove that the proposed MISO radar system incorporated with the KFSR algorithm achieves an azimuth superresolution of 20 times higher than that determined by the aperture size of the radar array.

In addition, to imitate real scenes, detection experiments are performed on complex N-, V-, and A-shaped targets, each composed of multitrihedral reflectors, as shown in Fig. 10. The imaging scenario and imaging results of the N-shaped, V-shaped, and A-shaped targets are depicted in Fig. 10(a)–(c), respectively. Therein, Fig. 10(i) shows the photographs of the imaging scenario, in which multitrihedral reflectors are placed forward along the detection path. First, the kernel function-based correlation algorithm is applied to process the received echoes; the imaging results are depicted in Fig. 10(ii), which exhibit aliasing and strong background noise, resulting in the inability to distinguish the multitargets in the range and azimuth directions. When the proposed KFSR algorithm is applied, the imaging area with a size of 0.47 m (range) $\times$ 0.87 m (azimuth) is divided into 47 (range) $\times$ 87 (azimuth) units. The reconstructed imaging results are depicted in Fig. 10(iii). Benefiting from the superresolution ability of the established radar system, the complex targets with N, V, and A shapes are clearly reconstructed, which match well with the real geometric features of the targets. These results verify the feasibility of the proposed photonics-based superresolution radar in forward-looking imaging again.

To quantitatively evaluate the imaging quality, the image entropy and image contrast from the imaging results in Fig. 10 are calculated. The image entropy assesses the overall quality of the entire image. The image contrast is used to capture the

Authorized licensed use limited to: NANJING UNIVERSITY OF AERONAUTICS AND ASTRONAUTICS. Downloaded on July 20,2026 at 09:35:34 UTC from IEEE Xplore. Restrictions apply.

TABLE II
COMPARISON OF IMAGING QUALITY BETWEEN DIFFERENT ALGORITHMS

Imaging scenarios	Algorithms			
	kernel function-based correlation algorithm		Proposed KSFR algorithm	
	Image entropy	Image contrast	Image entropy	Image contrast
N-shaped	6.77	0.62	0.06	8.68
V-shaped	6.91	0.75	0.05	10.95
A-shaped	6.99	0.55	0.07	9.94

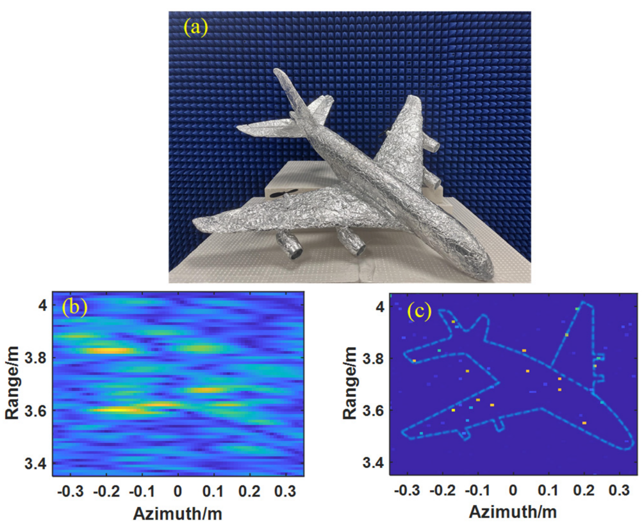

Fig. 11. (a) Photographs of the imaging scenario with an aircraft model, and the imaging results based on (b) kernel function-based correlation algorithm and (c) proposed KFSR algorithm.

local characteristics of the strong scattering points and reflect the focusing characteristics of the imaging result. The image entropy H_σ and image contrast C_σ are defined as follows [39]:

$$H_\sigma = -\sum_{l=1}^{L} \frac{\sigma_l}{\sum_l |\sigma_l|^2} \log \frac{\sigma_l}{\sum_l |\sigma_l|^2} \tag{14}$$

$$C_\sigma = \frac{\sqrt{\frac{1}{L}\sum_{l=1}^{L} |\sigma_l - \frac{1}{L}\sum_{l=1}^{L} |\sigma_l||^2}}{\frac{1}{L}\sum_{l=1}^{L} |\sigma_l|}. \tag{15}$$

In the experiment, the image entropy is calculated over the full image, while the image contrast is obtained using a target region within the red box marked in Fig. 10, which consists of 15 × 7 imaging grids. The corresponding results are listed in Table II. The KFSR algorithm achieves an imaging entropy of 0.05 and an image contrast of 10.95, whereas the kernel-based correlation method yields an imaging entropy of 6.77 and an image contrast of 0.75. These quantitative results demonstrate that the proposed KSFR algorithm exhibits superior imaging performance in terms of target focusing capability and resolution.

Furthermore, an additional imaging experiment is conducted using an aircraft model to simulate extended targets. Fig. 11(a) shows the photograph of the imaging scenario, where a 45 × 45 cm aircraft model wrapped in tin foil serves as the detected target. Fig. 11(b) presents the imaging result obtained using the kernel function-based correlation algorithm. Due to the limited azimuth resolution, the target cannot be clearly distinguished. When the proposed KFSR algorithm is applied, the imaging result is shown in Fig. 11(c). The imaging area with a size of 0.71 m (range) × 0.71 m (azimuth) is divided into 71 (range) × 71 (azimuth) units. Without loss of generality, a target illuminated by high-frequency electromagnetic waves can be modeled as a superposition of a finite number of dominant scattering points. Thus, the reconstructed image reveals a distribution of discrete strong scattering centers. By fitting the profile of the aircraft model, key structural components of the target, such as the nose, wing edges, engine inlets, and tail are clearly resolved, which aligns well with the geometric features of the aircraft model. Consequently, the proposed system could recover the fine scattering structure of complex targets, thereby offering a potential solution for target recognition and classification.

IV. CONCLUSION

In conclusion, we have proposed and experimentally demonstrated a photonics-based superresolution MISO radar imaging system. A broadband FH signal is generated based on the P1 oscillation dynamics of an optically injected semiconductor laser and transmitted through a ULA in a TDM manner. Benefiting from the large bandwidth of microwave photonics, the orthogonality between transmitted signals in different channels is guaranteed, so that the fluctuating characteristics of wavefront modulation are significantly expanded in the frequency domain. Thus, the diversity of the stochastic radiation field is extended to the space-time-frequency dimensions. Furthermore, a KFSR algorithm for superresolution imaging is proposed. In the experiments, a photonics-based 4 × 1 MISO radar with a bandwidth of 8 GHz (10–18 GHz) is successfully established. The radar system achieves superresolution imaging with an azimuth resolution 20 times higher than that of the traditional MISO radar. Superresolution imaging of complex targets is also demonstrated. These experimental results show the feasibility of the proposed radar system in forward-looking, high-resolution imaging. In subsequent research, optical or optoelectronic feedback mechanisms can be incorporated into the proposed system to improve the signal-to-noise ratio of the broadband signals. In addition, faster imaging algorithms, such as a deep expansion network, can be adopted to further enhance the system's practicality.

REFERENCES

[1] M. Skolnik, *Radar Handbook*, 3rd ed., New York, NY, USA: McGraw-Hill, 2008.
[2] I. Bekkerman and J. Tabrikian, "Target detection and localization using MIMO radars and sonars," *IEEE Trans. Signal Process.*, vol. 54, no. 10, pp. 3873–3883, Oct. 2006.
[3] A. Haimovich, R. Blum, and L. Cimini, "MIMO radar with widely separated antennas," *IEEE Signal Process. Mag.*, vol. 25, no. 1, pp. 116–129, Jan. 2008.
[4] Y. Cheng, X. Zhou, X. Xu, Y. Qin, and H. Wang, "Radar coincidence imaging with stochastic frequency modulated array," *IEEE J. Sel. Topics Signal Process.*, vol. 11, no. 2, pp. 414–427, Mar. 2017.

Authorized licensed use limited to: NANJING UNIVERSITY OF AERONAUTICS AND ASTRONAUTICS. Downloaded on July 20,2026 at 09:35:34 UTC from IEEE Xplore. Restrictions apply.

[5] D. Li, X. Li, Y. Qin, Y. Cheng, and H. Wang, "Radar coincidence imaging: An instantaneous imaging technique with stochastic signals," *IEEE Trans. Geosci. Remote Sens.*, vol. 52, no. 4, pp. 2261–2277, Apr. 2014.

[6] L. C. Potter, E. Ertin, J. T. Parker, and M. Cetin, "Sparsity and compressed sensing in radar imaging," *Proc. IEEE*, vol. 98, no. 6, pp. 1006–1020, Jun. 2010.

[7] Q. Zhang, G. Zhang, N. Chen, Q. Xiong, J. Xie, and Y. He, "Waveform design of radar coincidence imaging radiation field based on image entropy," *Electron. Lett.*, vol. 60, no. 10, pp. e1320–1, May 2024.

[8] K. Cao, Y. Cheng, Q. Liu, and H. Wang, "Microwave coincidence imaging based on attributed scattering model," *IEEE Signal Process. Lett.*, vol. 29, pp. 1694–1698, 2022.

[9] K. Cao, Y. Cheng, K. Liu, H. Wang, J. Wang, and H. Liu, "Off-grid microwave coincidence imaging based on directional grid fission," *IEEE Antennas Wireless Propag. Lett.*, vol. 19, pp. 2497–2501, 2020.

[10] J. Yao, "Microwave photonics," *J. Lightw. Technol.*, vol. 27, no. 3, pp. 314–335, Feb. 2009.

[11] J. Capmany and D. Novak, "Microwave photonics combines two worlds," *Nature Photon.*, vol. 1, no. 6, pp. 319–330, Jun. 2007.

[12] S. S. S. Panda, T. Panigrahi, S. R. Parne, S. L. Sabat, and L. R. Cenkeramaddi, "Recent advances and future directions of microwave photonic radars: A review," *IEEE Sensors J.*, vol. 21, no. 19, pp. 21144–21158, Oct. 2021.

[13] S. Pan and Y. Zhang, "Microwave photonic radars," *J. Lightw. Technol.*, vol. 38, no. 19, pp. 5450–5484, Oct. 2020.

[14] P. Ghelfi et al., "Photonics in radar systems: RF integration for state-of-the-art functionality," *IEEE Microw. Mag.*, vol. 16, no. 8, pp. 74–83, Sep. 2015.

[15] S. Pan, X. Ye, Y. Zhang, and F. Zhang, "Microwave photonic array radars," *IEEE J. Microw.*, vol. 1, no. 1, pp. 176–190, Jan. 2021.

[16] B. Gao, F. Zhang, E. Zhao, D. Zhang, and S. Pan, "High-resolution phased array radar imaging by photonics-based broadband digital beamforming," *Opt. Express.*, vol. 27, no. 9, p. 13194, Apr. 2019.

[17] D. Bleh et al., "W -band time-domain multiplexing FMCW MIMO radar for far-field 3-D imaging," *IEEE Trans. Microw. Theory Techn.*, vol. 65, no. 9, pp. 3474–3484, Sep. 2017.

[18] Y. Zhou, F. Zhang, J. Kong, and S. Pan, "High-resolution 3D imaging by microwave photonic time division multiplexing-multiple-input-multiple-output radar with broadband digital beamforming," *IET Radar, Sonar Navigat.*, vol. 18, no. 9, pp. 1531–1540, May 2024.

[19] F. Zhang, G. Sun, Y. Zhou, B. Gao, and S. Pan, "Towards high-resolution imaging with photonics-based time division multiplexing MIMO radar," *IEEE J. Sel. Topics Quantum Electron.*, vol. 28, no. 5, pp. 1–10, Sep. 2022.

[20] B. Gao, F. Zhang, G. Sun, Y. Xiang, and S. Pan, "Microwave photonic MIMO radar for high-resolution imaging," *J. Lightw. Technol.*, vol. 39, no. 24, pp. 7726–7733, Dec. 15, 2021.

[21] T. Yao, D. Zhu, D. Ben, and S. Pan, "Distributed MIMO chaotic radar based on wavelength-division multiplexing technology," *Opt. Lett.*, vol. 40, no. 8, pp. 1631–1634, Apr. 2015.

[22] F. Zhang, B. Gao, and S. Pan, "Broadband array radar based on microwave photonic frequency multiplication and de-chirp receiving," *Infr. Laser Eng.*, vol. 50, no. 7, Jul. 2021, Art. no. 20211051.

[23] Y. Zhang, H. Wu, D. Zhu, and S. Pan, "An optically controlled phased array antenna based on single sideband polarization modulation," *Opt. Exp.*, vol. 22, no. 4, pp. 3761–37654, Feb. 2014.

[24] Y. Deng, A. Burr, and G. White, "Performance of MIMO systems with combined polarization multiplexing and transmit diversity," in *Proc. IEEE 61st Veh. Technol. Conf.*, vol. 2, Stockholm, Sweden, Jun. 2005, pp. 869–873.

[25] G. Sun, Y. Zhou, Y. He, X. Yu, F. Zhang, and S. Pan, "Photonics-based MIMO radar with broadband digital coincidence imaging," *IEEE Trans. Microw. Theory Techn.*, vol. 72, no. 12, pp. 6996–7003, Dec. 2024.

[26] T. B. Simpson, J. M. Liu, K. F. Huang, and K. Tai, "Nonlinear dynamics induced by external optical injection in semiconductor lasers," *Quantum Semiclass. Opt., J. Eur. Opt. Soc. B*, vol. 9, no. 5, pp. 765–784, Oct. 1997.

[27] X. Yu et al., "Frequency-tunable narrow linewidth THz signal generation by semiconductor lasers subject to mutual optical injection," in *Proc. Asia Commun. Photon. Conference/Int. Photon. Optoelectronics Meetings (ACP/POEM)*, Wuhan, China, Nov. 2023, pp. 1–3.

[28] S.-C. Chan, S.-K. Hwang, and J.-M. Liu, "Period-one oscillation for photonic microwave transmission using an optically injected semiconductor laser," *Opt. Exp.*, vol. 15, no. 22, p. 14921, Oct. 2007.

[29] X. Yu et al., "Broadband stepped-frequency radar waveform generation by Fourier domain mode-locking period-one laser dynamics," *Opt. Lett.*, vol. 49, no. 15, pp. 4266–4269, Jul. 2024.

[30] X. Yu et al., "Microwave generation by P2 dynamics of optically injected semiconductor laser," *J. Lightw. Technol.*, vol. 43, no. 10, pp. 4895–4902, May 1, 2025.

[31] J. S. Suelzer, T. B. Simpson, P. Devgan, and N. G. Usechak, "Tunable, low-phase-noise microwave signals from an optically injected semiconductor laser with opto-electronic feedback," *Opt. Lett.*, vol. 42, no. 16, pp. 3181–3184, Aug. 2017.

[32] X. Yu et al., "Broadband frequency-hopping radar with Fourier domain mode-locking period-one laser dynamics," *IEEE Photon. Technol. Lett.*, vol. 37, no. 19, pp. 1105–1108, Oct. 15, 2025.

[33] S.-K. Hwang, J.-M. Liu, and J. K. White, "Characteristics of period-one oscillations in semiconductor lasers subject to optical injection," *IEEE J. Sel. Topics Quantum Electron.*, vol. 10, no. 5, pp. 974–981, Sep. 2004.

[34] X. Zhou, H. Wang, Y. Cheng, Y. Qin, and H. Chen, "Radar coincidence imaging for off-grid target using frequency-hopping waveforms," *Int. J. Antennas Propagation.*, vol. 2016, pp. 1–16, 2016.

[35] C. Oliver, "Synthetic-aperture radar imaging," *J. Phys. D, Appl. Phys.*, vol. 22, no. 7, pp. 871–890, 1989.

[36] Z. Liao, D. Lu, J. Hu, and J. Zhang, "Computationally efficient range profile synthesis method based on zero-padding inverse discrete Fourier transform for random stepped frequency radar," *J. Appl. Remote Sens.*, vol. 13, no. 1, Jan. 2019, Art. no. 016505.

[37] S. S. Chen, D. L. Donoho, and M. A. Saunders, "Atomic decomposition by basis pursuit," *SIAM J. Sci. Comput.*, vol. 20, no. 1, pp. 33–61, 1998.

[38] Z. Chen, J. Tang, X. Zhang, D. K. C. So, S. Jin, and K. K. Wong, "Hybrid evolutionary-based sparse channel estimation for IRS-assisted mmWave MIMO systems," *J. Appl. Remote Sens.*, vol. 10, no. 2, May 2016, Art. no. 025009.

[39] G. Xu, Y. Chen, A. Ji, B. Zhang, C. Yu, and W. Hong, "3-D high-resolution imaging and array calibration of ground-based millimeter-wave MIMO radar," *IEEE Trans. Microw. Theory Techn.*, vol. 72, no. 8, pp. 4919–4931, Aug. 2024.

Authorized licensed use limited to: NANJING UNIVERSITY OF AERONAUTICS AND ASTRONAUTICS. Downloaded on July 20,2026 at 09:35:34 UTC from IEEE Xplore. Restrictions apply.